Electronic Supplementary Material (ESI) for Physical Chemistry Chemical Physics.

Supporting Information

Effect of the Degree of Inversion on Optical Properties of Spinel $ZnFe_2O_4$

Luis I. Granone[a,b], Anna C. Ulpe[c], Lars Robben[d,e], Stephen Klimke[f], Moritz Jahns[f], Franz Renz[f], Thorsten M. Gesing[d,e], Thomas Bredow[c], Ralf Dillert[a,b], Detlef W. Bahnemann[a,b,g]

[a]Institute of Technical Chemistry, Gottfried Wilhelm Leibniz University Hannover, Callinstrasse 3, D-30167 Hannover, Germany.

[b]Laboratory of Nano- and Quantum-Engineering (LNQE), Gottfried Wilhelm Leibniz University Hannover, Schneiderberg 39, D-30167 Hannover, Germany.

[c]Universität Bonn, Mulliken Center for Theoretical Chemistry, Institut für Physikalische und Theoretische Chemie, Beringstrasse 4, D-53115 Bonn, Germany.

[d]University of Bremen, Institute of Inorganic Chemistry and Crystallography, Leobener Strasse 7, D-28359 Bremen, Germany.

[e]University of Bremen, MAPEX Center for Materials and Processes, Bibliothekstrasse 1, D-28359 Bremen, Germany.

[f]Institute for Inorganic Chemistry, Gottfried Wilhelm Leibniz University Hannover, Callinstrasse 9, D-30167 Hannover, Germany.

[g]Laboratory "Photoactive Nanocomposite Materials", Saint-Petersburg State University, Ulyanovskaya str. 1, 198504 Peterhof, Saint-Petersburg, Russian Federation.

Rietveld plots of zinc ferrite samples

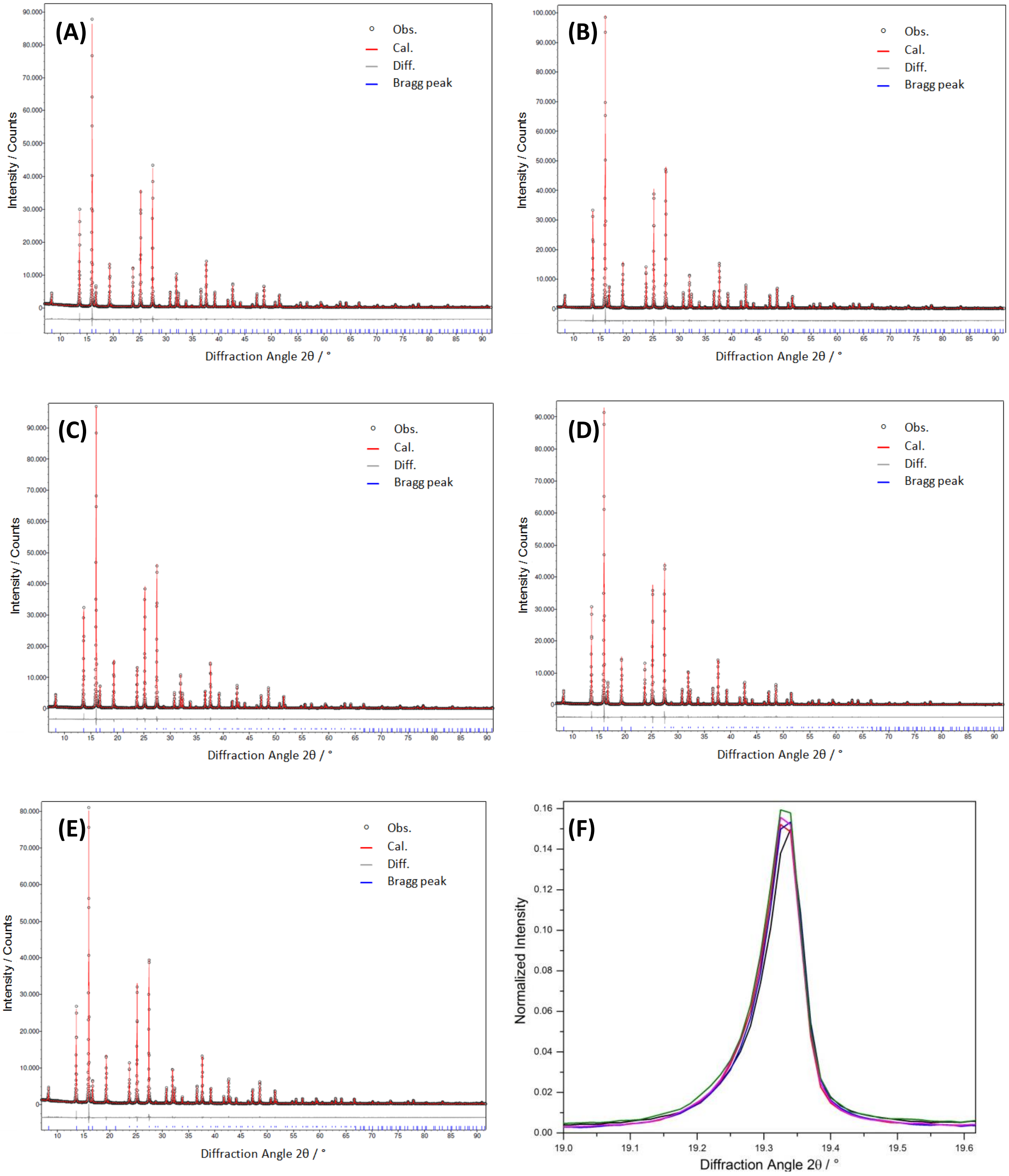

Fig. S1. Rietveld plots of the ZFO samples after calcination at **(A)** 773 K, **(B)** 873 K, **(C)** 973 K, **(D)** 1073 K, and **(E)** 1173 K. Monochromatized MoKα_1 radiation was used for the measurement. **(F)** Magnification of the diffraction peak at 19.33° of the different ZFO samples: — ZFO_773, x = 0.074 ± 0.011; — ZFO_873, x = 0.104 ± 0.013; — ZFO_973, x = 0.134 ± 0.008; — ZFO_1073, x = 0.159 ± 0.010; — ZFO_1173, x = 0.203 ± 0.017. The diffractograms were normalized to the main diffraction peak at 16.01°. An increase in the relative intensity is observed as the degree of inversion increases from 0.07 to 0.20.

Mössbauer spectra of zinc ferrite samples and γ-Fe_2O_3

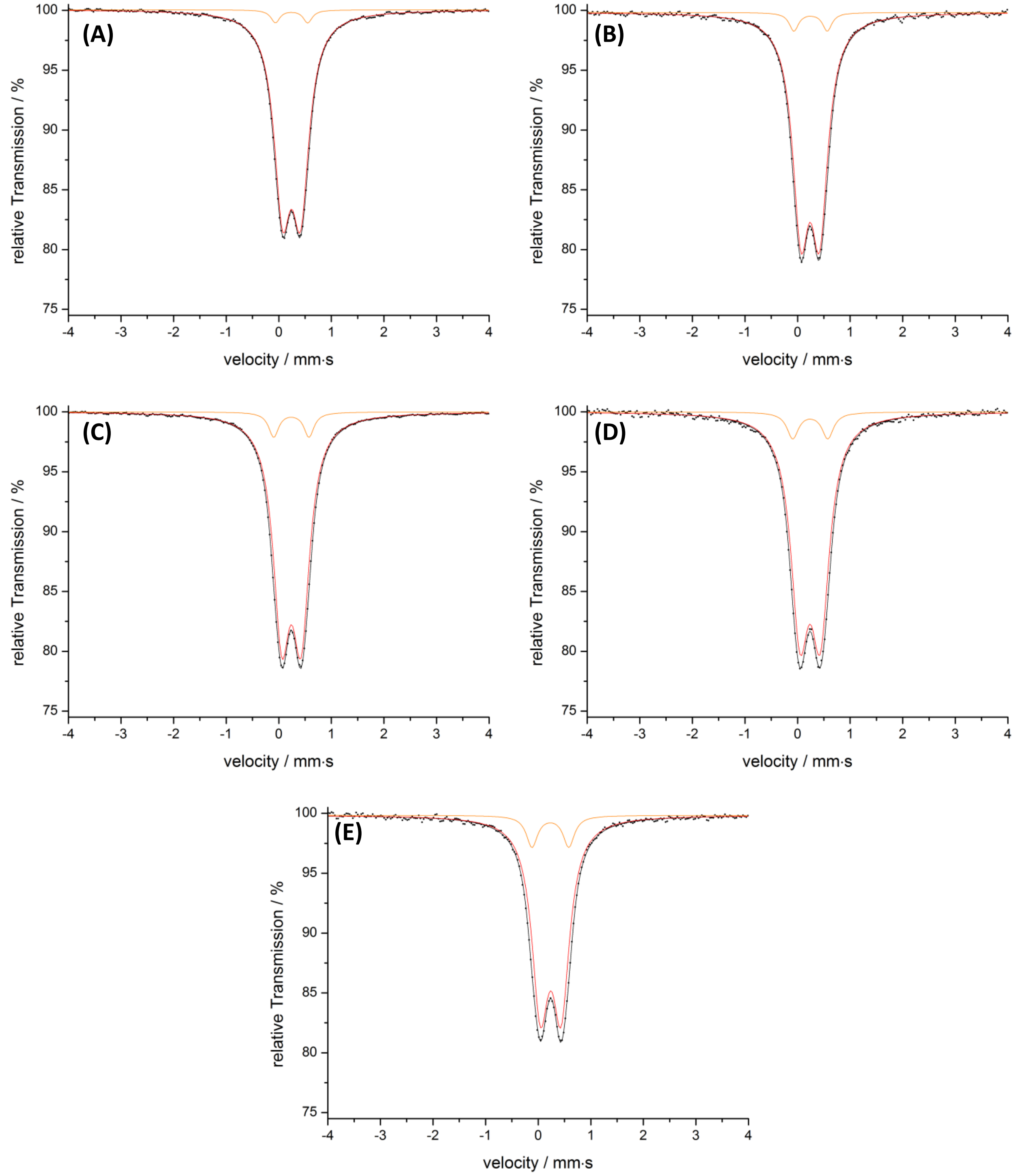

Fig. S2. Mössbauer spectra of the ZFO samples after calcination at **(A)** 773 K, **(B)** 873 K, **(C)** 973 K, **(D)** 1073 K, and **(E)** 1173 K. The black line represents the cumulative peak fit consisting of the orange and red lines.

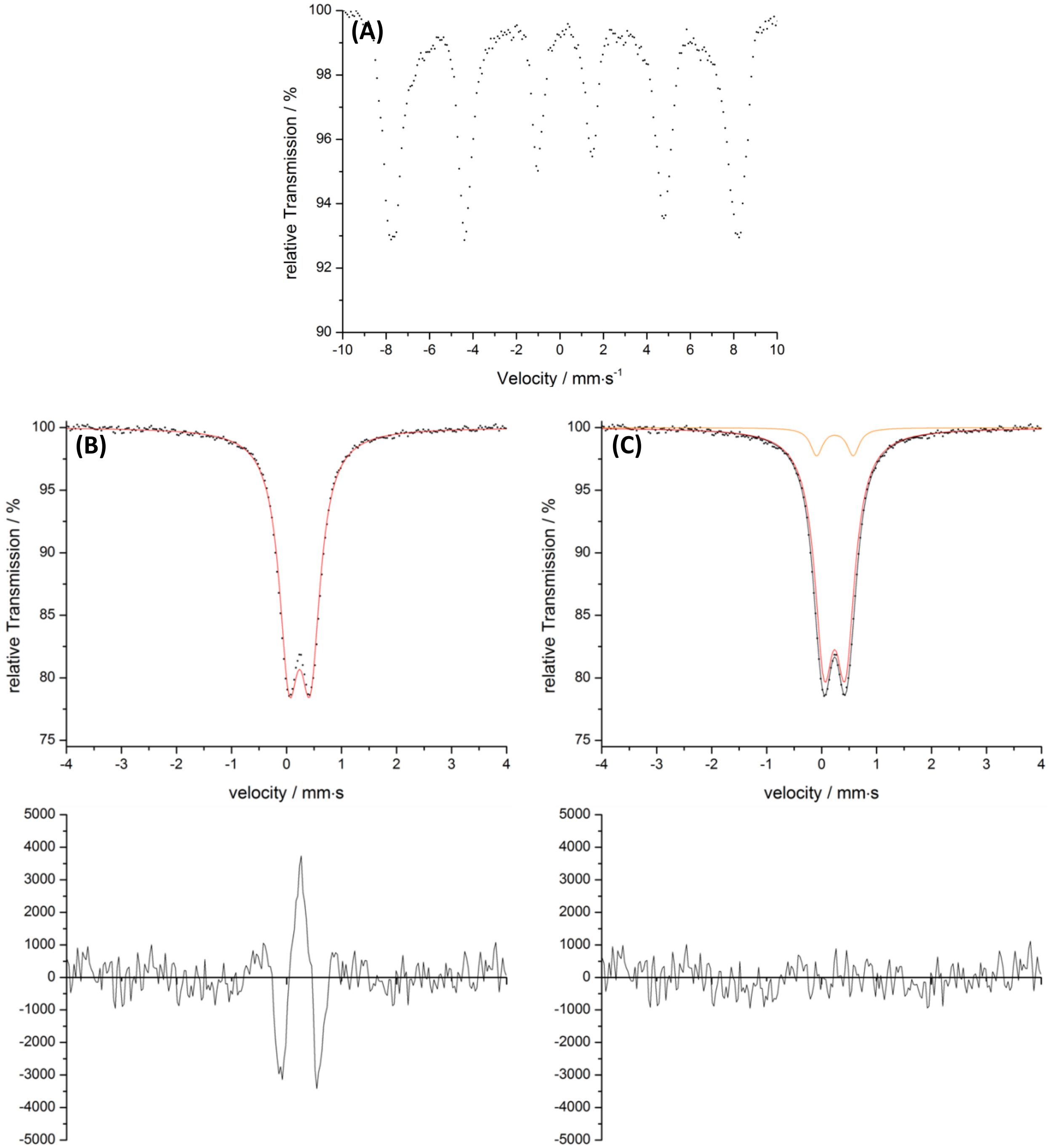

Fig. S3. **(A)** Mössbauer spectrum of a commercial γ-Fe_2O_3 sample (20-40 nm, io·li·tec). **(B-C)** Fitted Mössbauer spectrum and residual plot of ZFO_1073 obtained by considering **(B)** one and **(C)** two paramagnetic doublets. Similar results are observed for the rest of the ZFO samples.

Table S1. Mössbauer parameters of the ZFO samples with different calcination temperatures. δ_{IS}, Δ_Q, FWHM are the isomer shift, quadrupole splitting, and full width at half maximum, respectively.

Calcination temperature / K	δ_{IS} / mm·s^{-1}	Δ_Q /mm·s^{-1}	FWHM / mm·s^{-1}	Population / %
773	0.354 ± 0.001	0.344 ± 0.002	0.193 ± 0.001	96.3 ± 0.85
	0.353 ± 0.008	0.614 ± 0.023	0.103 ± 0.010	3.7 ± 0.74
873	0.352 ± 0.001	0.355 ± 0.003	0.190 ± 0.002	94.9 ± 1.2
	0.358 ± 0.009	0.634 ± 0.025	0.108 ± 0.019	5.1 ± 1.0
973	0.352 ± 0.001	0.369 ± 0.001	0.195 ± 0.001	93.2 ± 0.5
	0.349 ± 0.003	0.671 ± 0.008	0.116 ± 0.007	6.8 ± 0.5
1073	0.349 ± 0.002	0.387 ± 0.023	0.208 ± 0.006	92.2 ± 0.63
	0.352 ± 0.008	0.666 ± 0.071	0.133 ± 0.063	7.8 ± 0.58
1173	0.349 ± 0.002	0.395 ± 0.003	0.195 ± 0.003	89.5 ± 1.5
	0.343 ± 0.007	0.699 ± 0.014	0.129 ± 0.015	10.5 ± 1.4

The Mössbauer measurements were fitted by using one and two paramagnetic doublets. A comparison of the two spectra showed that a single doublet leads to a bigger deviation between the observed signals and the Lorentzian fit (Fig. S3(B) and (C)). Similar signals were observed by H. Ehrhardt *et al.*[1] and similar values for the isomer shift and the quadrupole splitting were obtained. The difference between the quadrupole splitting and the FWHM of the two doublets can be explained by the different lattice sites of the iron. It is well known that the quadrupole splitting of tetrahedral sites of non-magnetic spinel type oxides are larger compared to the octahedral sites.[2,3] Furthermore, the tetrahedral sites show different bond length and a smaller distribution compared to the octahedral sites in the crystals which leads to smaller influence of surface defects and therefore smaller values for the FWHM which are still bigger than the natural line width.

Configurational entropy of zinc ferrite

Considering that the change in the non-configurational entropy associated with the disordering process is negligible,[4] the total entropy is defined by the configurational entropy (S_C) alone.

$$S_C = -R \sum_{s=1}^{2} \sum_{i=1}^{2} b^s N_i^s ln N_i^s \tag{1}$$

$$S_C = -R \left[x \ln x + (1-x) \ln(1-x) + (2-x) \ln\left(1 - \frac{x}{2}\right) + x \ln \frac{x}{2} \right] \tag{2}$$

where N_i^s is the fraction of species i (i = 1 for Fe and i = 2 for Zn) in site s (s = 1 for tetrahedral sites and s = 2 for octahedral sites), b^s is the number of sites of type s per formula unit, and x is the degree of inversion. From a plot of S_C vs. x (Fig. S4) it can be seen that S_c tends to 0 at x = 0, increases to a maximum at the random arrangement of x = 2/3, and then decreases towards $2R \ln 2$ for x = 1. The change in the Gibbs free energy for the disordering process, ΔG_D°, is defined as

$$\Delta G_D^{\circ} = \Delta H_D^{\circ} - T \Delta S_C^{\circ} \tag{3}$$

where ΔH_D° and ΔS_D° are the changes in enthalpy and entropy, respectively, associated with the cation distribution process, and T is the temperature. Since S_C° = 0 when x = 0, then:

$$\Delta S_C^{\circ} = S_C = -R \left[x \ln x + (1-x) \ln(1-x) + x \ln \frac{x}{2} + (2-x) \ln\left(1 - \frac{x}{2}\right) \right] \tag{4}$$

Considering that ΔH_D° is T and x independent, it is clear that at high temperatures the process becomes entropy dependent and the degree of inversion increases towards the maximum of $x = 2/3$. O'Neill and Navrotsky[5,6] showed, from lattice energy arguments, that ΔH_D° depends linearly on x. Nevertheless, it also emerges from this more comprehensive model that the degree of inversion increases with higher calcination temperatures, as is observed from the experimental results.

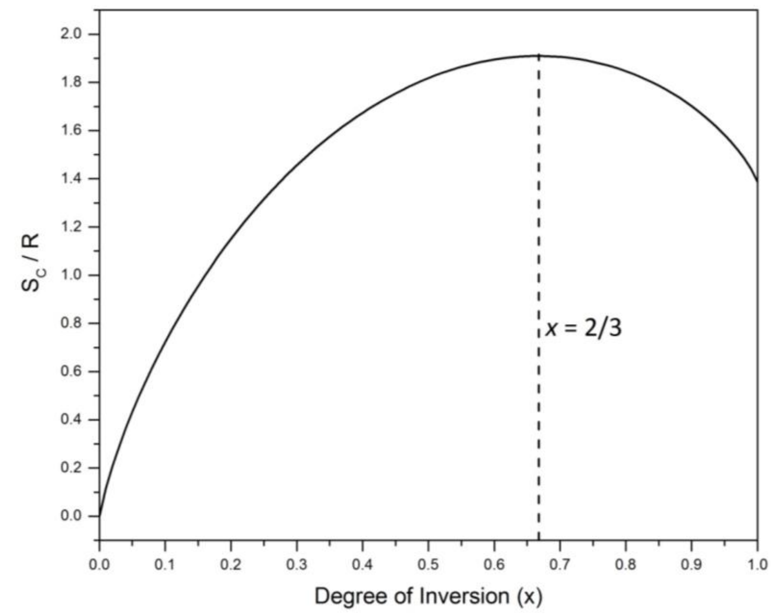

Fig. S4. Plot of the configurational entropy, S_C, of ZFO vs. the degree of inversion, x. S_c tends to 0 at $x = 0$, increases to a maximum at the random arrangement of $x = 2/3$, and then decreases towards $2R \ln 2$ for $x = 1$.

Raman spectra of zinc ferrite samples

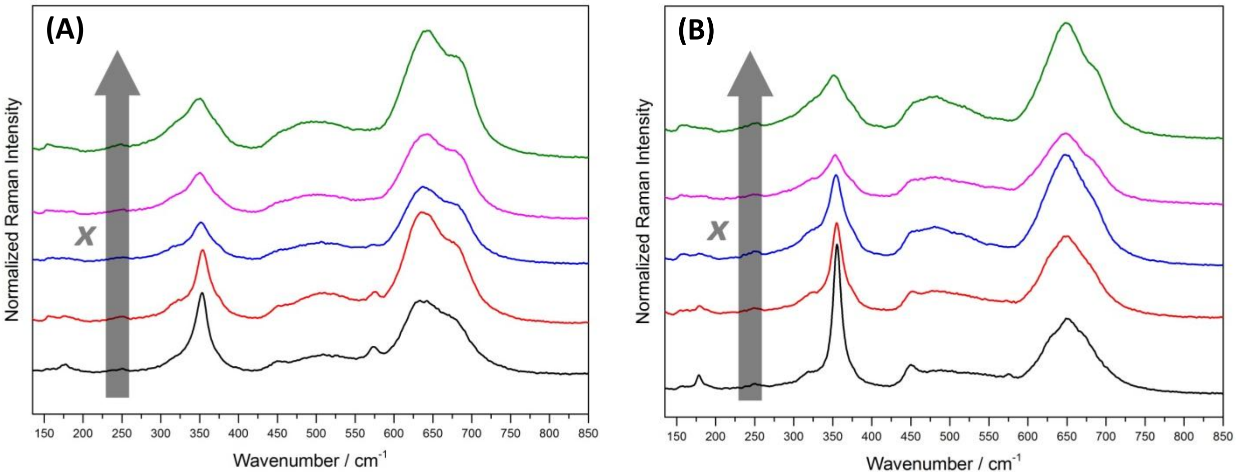

Fig. S5. Normalized Raman spectra of the ZFO samples with increasing degree of inversion (— ZFO_773, $x = 0.074 \pm 0.011$; — ZFO_873, $x = 0.104 \pm 0.013$; — ZFO_973, $x = 0.134 \pm 0.008$; — ZFO_1073, $x = 0.159 \pm 0.010$; — ZFO_1173, $x = 0.203 \pm 0.017$) obtained using **(A)** a 532 nm and **(B)** a 633 nm laser as the excitation source.

Comparison between the Raman spectra of zinc ferrite ($x \approx 0.073$) and of γ-Fe_2O_3

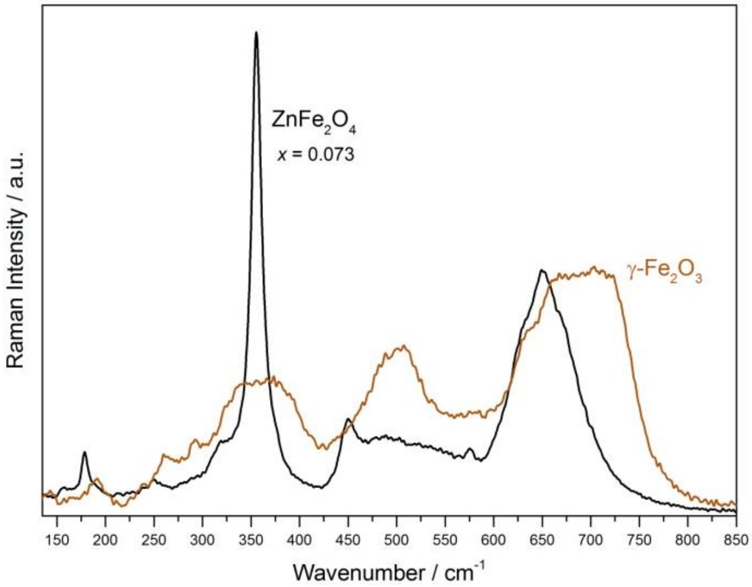

Fig. S6. Raman spectrum of a commercial γ-Fe_2O_3 sample (brown line) obtained using a 633 nm laser excitation. The Raman spectrum of ZFO_773 (black line) is included for comparison. Although most of the ZFO and γ-Fe_2O_3 Raman scattering signals are superimposed, the absence of a shoulder at ca. 718 cm^{-1} in the ZFO spectrum proves that γ-Fe_2O_3 is not present as an impurity phase.

Deconvolution of the broad Raman signal at 647 ± 3 cm^{-1}

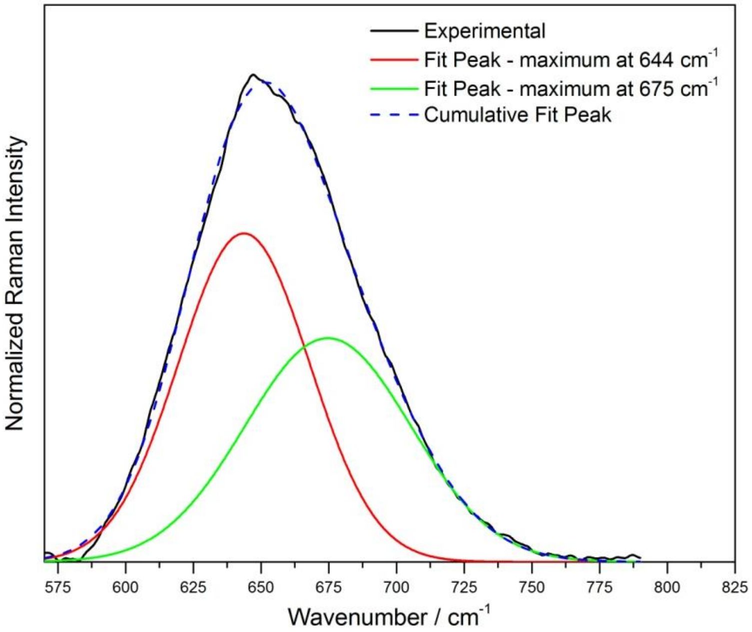

Fig. S7. Deconvolution of the broad Raman signal at 647 ± 3 cm^{-1} (679 nm laser excitation) using Gaussian-shape curves with maxima located at ca. 644 cm^{-1} and 675 cm^{-1}.

Correlation between intensity of the Raman signals and the degree of inversion

The intensity ratio between the Raman signals serves as a reference to estimate the degree of inversion of ZFO samples. Fig. 4 shows plots of the intensity ratio between the Raman shifts at 352 and 647 cm^{-1} (measured using a 785 nm, A, 633 nm, B, and 532 nm, C, laser as the excitation sources) as a function of the degree of inversion. The experimental data were fitted using an exponential decay function. To ascertain the validity of this empirical equation, the intensity ratio between the shifts at 352 and 647 cm^{-1} of a Raman spectrum presented by Wang *et al.*[7] was analyzed. For the ZFO sample with a reported degree of inversion of 0.10, a ratio of 3.02 was calculated. With this ratio and the equation given in Figure 4, a degree of inversion of 0.12 ± 0.03 was calculated, thus being in reasonable agreement with the value give by Wang *et al*.

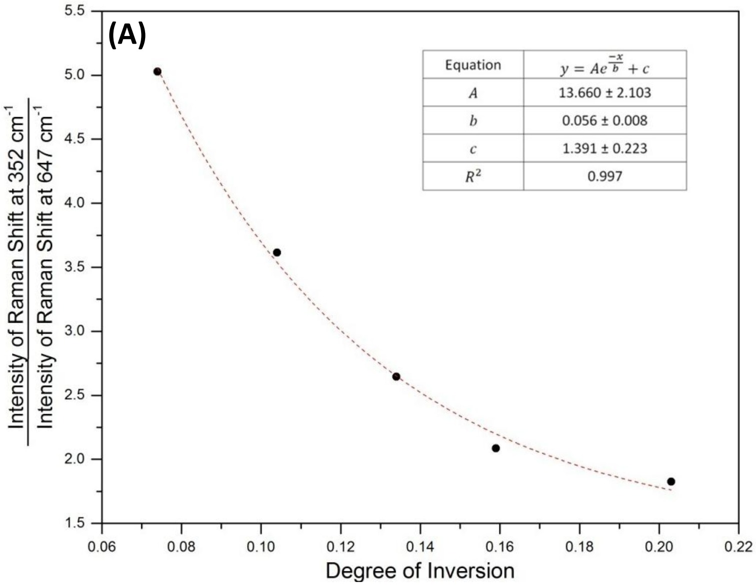

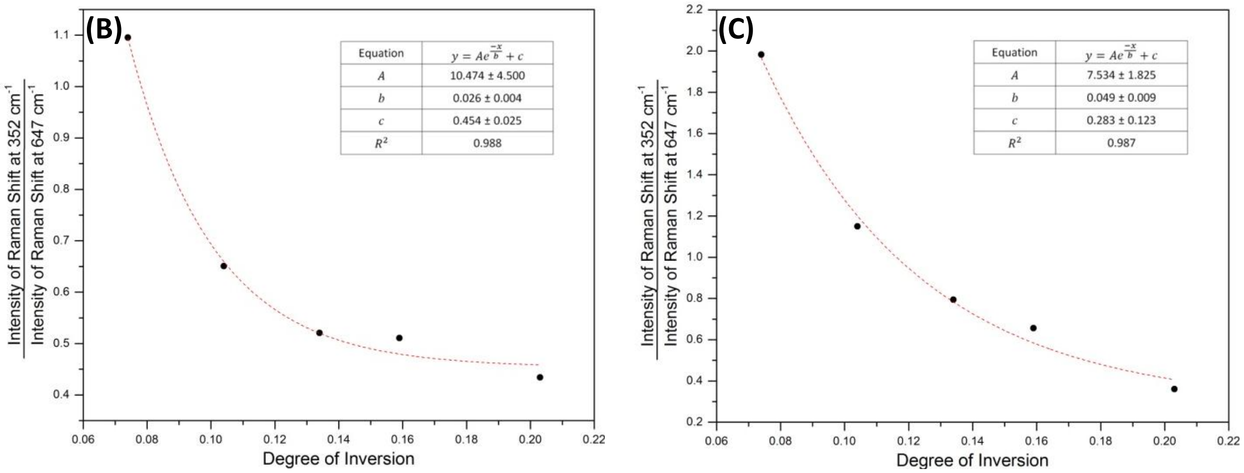

Fig. S8. Intensity ratio between the Raman shifts at 352 and 647 cm^{-1} (measured using **(A)** a 785 nm, **(B)** a 633 nm, and **(C)** a 532 nm laser as the excitation source) as a function of the degree of inversion. The insert shows the parameters of the exponential decay function used to fit the experimental data.

Photograph of zinc ferrite samples

Fig. S9. Photograph of the ZFO samples with different degrees of inversion (*x* = 0.074 ± 0.011, 0.104 ± 0.013, 0.134 ± 0.008, 0.159 ± 0.010, and 0.203 ± 0.017 for ZFO_773, ZFO_873, ZFO_973, ZFO_1073, and ZFO_1173, respectively). As the degree of inversion increases, the brownish orange color of the samples becomes gradually darker.

Identification and prediction of electronic transitions of zinc ferrite

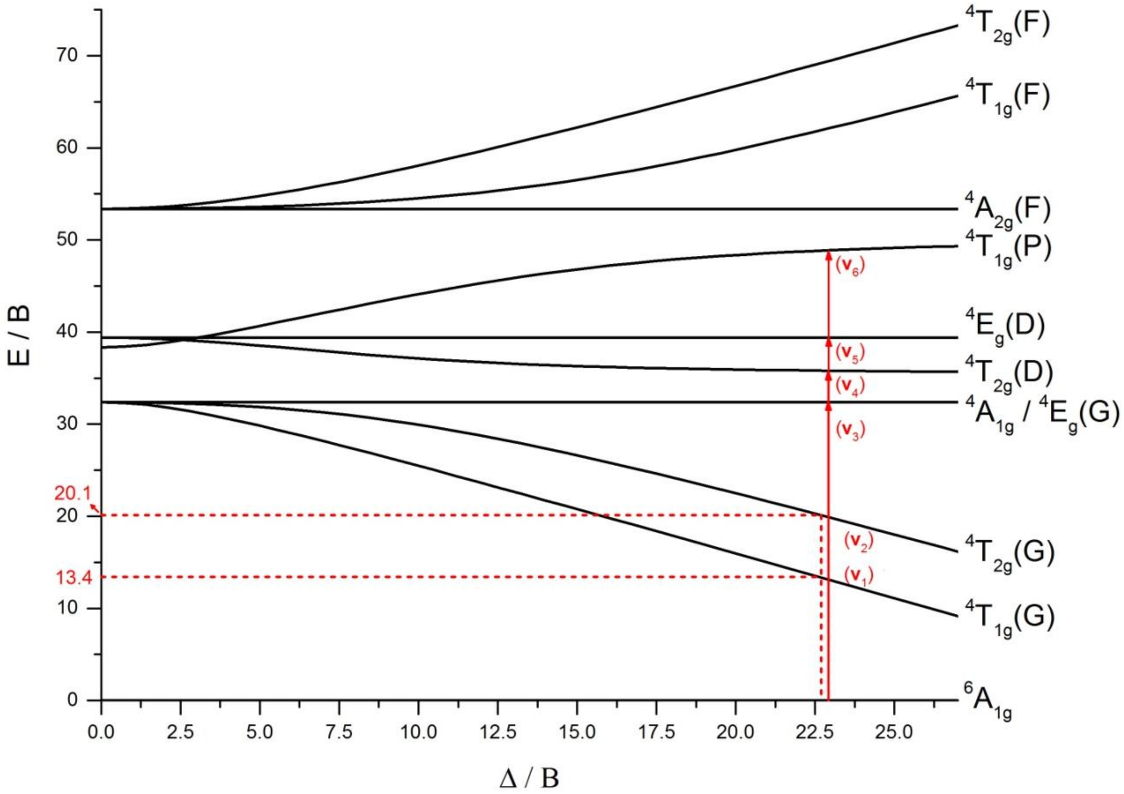

Fig. S10. Partial Tanabe-Sugano diagram for a high spin d^5 ion with octahedral symmetry. Only the excited states with spin multiplicity 4 are shown.

From an analysis based on the Tanabe-Sugano diagram for high spin d^5 octahedrally coordinated Fe^{3+} ions it is possible to obtain important parameters such as energy of the crystal field, Δ, for the FeO_6 octahedra and the Racah parameter. Moreover, predictions concerning the possible electronic transitions can be done.

The bands observed experimentally at 1200 nm (8333.3 cm^{-1}) and 795 nm (12578.6 cm^{-1}) can be assigned to the $^6A_{1g} \rightarrow {}^4T_{1g}(G)$ (ν_1) and $^6A_{1g} \rightarrow {}^4T_{2g}(G)$ (ν_2) transitions, respectively. The ration between the energy of these transitions is:

$$\frac{\nu_2}{\nu_1} = \frac{12578.6\ cm^{-1}}{8333.3\ cm^{-1}} \approx 1.5$$

A theoretical ratio of 1.5 between the energy of transitions ν_2 and ν_1 is observed in the Tanabe-Sugano diagram at a value of Δ/B of 22.7.

$$\frac{\Delta}{B} = 22.7 \rightarrow \frac{E_{\nu_2}/B}{E_{\nu_1}/B} = \frac{E_{\nu_2}}{E_{\nu_1}} = \frac{20.1}{13.4} = 1.5 \tag{S1}$$

where E_{ν_1} and E_{ν_2} are the energies of transitions ν_1 and ν_2, respectively, and B is the Racah parameter. B can be calculated as:

$$\frac{E_{\nu_2}}{B} = 20.1 \rightarrow B = \frac{12578.6\ cm^{-1}}{20.1} \approx 626\ cm^{-1} \tag{S2}$$

$$\frac{E_{\nu_1}}{B} = 13.4 \rightarrow B = \frac{8333.3\ cm^{-1}}{13.4} \approx 622\ cm^{-1} \tag{S3}$$

obtaining an average value of 624 cm^{-1}. The energy of the crystal field, Δ, can be obtained from:

$$\frac{\Delta}{B} = 22.7 = \frac{\Delta}{624cm^{-1}} \rightarrow \Delta \approx 14164cm^{-1} \tag{S4}$$

Finally, the energy of transitions ν_3, ν_4, ν_5, and ν_6 can be predicted from the Tanabe-Sugano diagram. The following values are obtained for these transitions:

Transition	Energy
$^6A_{1g} \rightarrow {}^4A_{1g}(G)$ (ν_3)	20248 cm^{-1} (494 nm / 2.51 eV)
$^6A_{1g} \rightarrow {}^4T_{2g}(D)$ (ν_4)	22300 cm^{-1} (448 nm / 2.76 eV)
$^6A_{1g} \rightarrow {}^4E_g(D)$ (ν_5)	24592 cm^{-1} (407 nm / 3.05 eV)
$^6A_{1g} \rightarrow {}^4T_{1g}(P)$ (ν_6)	30445 cm^{-1} (328 nm / 3.8 eV)

Application of DASF method to diffuse reflectance measurements

According to the absorption spectrum fitting (ASF) presented by Souri and Shomalian:[5,6]

$$\alpha = B(hc)^{m-1}\lambda\left(\frac{1}{\lambda}-\frac{1}{\lambda_g}\right)^m \tag{1}$$

where α is the absorption coefficient, λ is the wavelength, B is an empirical constant, h is Plank's constant, c is the velocity of light, λ_g is the wavelength corresponding to the optical band gap, and m is the index which can have different values (1/2, 2/3, 2, or 3) according to the type of transition.

The absorption coefficient α is related to the reflectance of a sample by the Kubelka-Munk radiative transfer model:[7]

$$f(R) = \frac{(1-R)^2}{2R} = \frac{\alpha}{s} \tag{2}$$

$$\alpha = f(R)\,s \tag{3}$$

where *f(R)* is the Kubelka-Munk function, *R* is the reflectance, and *s* is the scattering coefficient.

By combining equations (1) and (3):

$$f(R)s = B(hc)^{m-1}\lambda\left(\frac{1}{\lambda}-\frac{1}{\lambda_g}\right)^m \tag{4}$$

and considering that *s* is wavelength independent, the DASF method is deduced as follows:

$$\frac{f(R)s}{\lambda} = B(hc)^{m-1}\left(\frac{1}{\lambda}-\frac{1}{\lambda_g}\right)^m \tag{5}$$

$$\ln\left[\frac{f(R)s}{\lambda}\right] = \ln\left[B(hc)^{m-1}\lambda\left(\frac{1}{\lambda}-\frac{1}{\lambda_g}\right)^m\right] \tag{6}$$

$$\ln\left[\frac{f(R)}{\lambda}\right] + \ln s = \ln[B(hc)^{m-1}] + m\ln\left(\frac{1}{\lambda}-\frac{1}{\lambda_g}\right) \tag{7}$$

$$\mathrm{d}\left\{\ln\left[\frac{f(R)}{\lambda}\right] + \ln s\right\} = \mathrm{d}\left\{\ln[B(hc)^{m-1}] + m\ln\left(\frac{1}{\lambda}-\frac{1}{\lambda_g}\right)\right\} \tag{8}$$

$$d\left\{\ln\left[\frac{f(R)}{\lambda}\right]\right\} = d\left\{m\ln\left(\frac{1}{\lambda}-\frac{1}{\lambda_g}\right)\right\} \tag{9}$$

$$d\left\{\ln\left[\frac{f(R)}{\lambda}\right]\right\} = \frac{\mathrm{m}}{\left(\frac{1}{\lambda}-\frac{1}{\lambda_g}\right)}\,\mathrm{d}\left(\frac{1}{\lambda}\right) \tag{10}$$

$$\boldsymbol{\frac{d\left\{\ln\left[\frac{f(R)}{\lambda}\right]\right\}}{\mathrm{d}\left(\frac{1}{\lambda}\right)} = \frac{\mathrm{m}}{\left(\frac{1}{\lambda}-\frac{1}{\lambda_g}\right)}} \tag{11}$$

Eq. 11 is the DASF equivalent for diffuse reflectance measurements. However, *f(R)* can only be used instead of α when a wavelength independent scattering coefficient is assumed.

SEM pictures of the ZFO samples

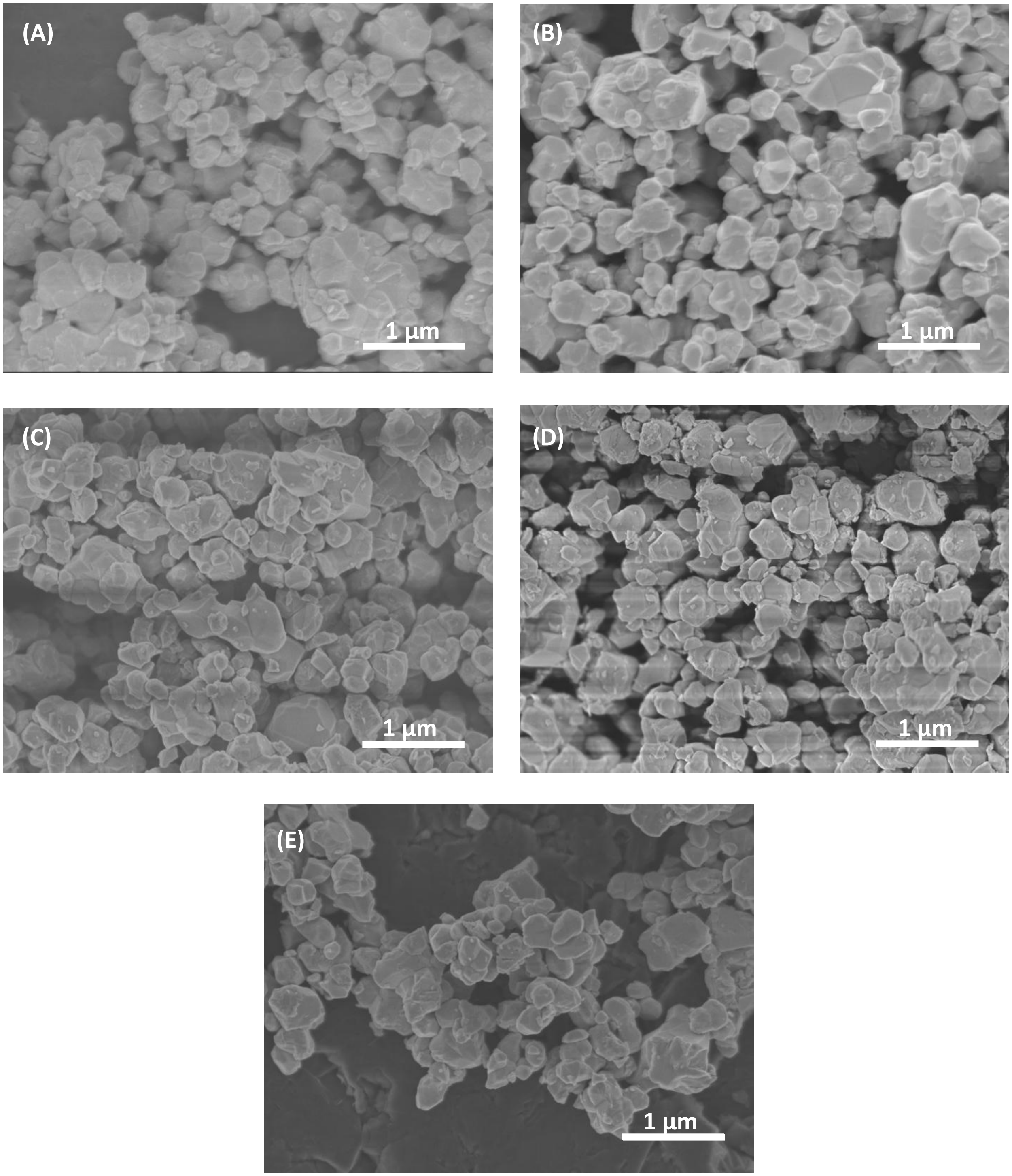

Fig. S11. SEM images of the ZFO samples after calcination at (A) 773 K, (B) 873 K, (C) 973 K, (D) 1073 K, and (E) 1173 K. Similar particle size and morphology are observed between the samples annealed at different temperatures.

DASF analysis of zinc ferrite sample with $x = 0.074 \pm 0.011$

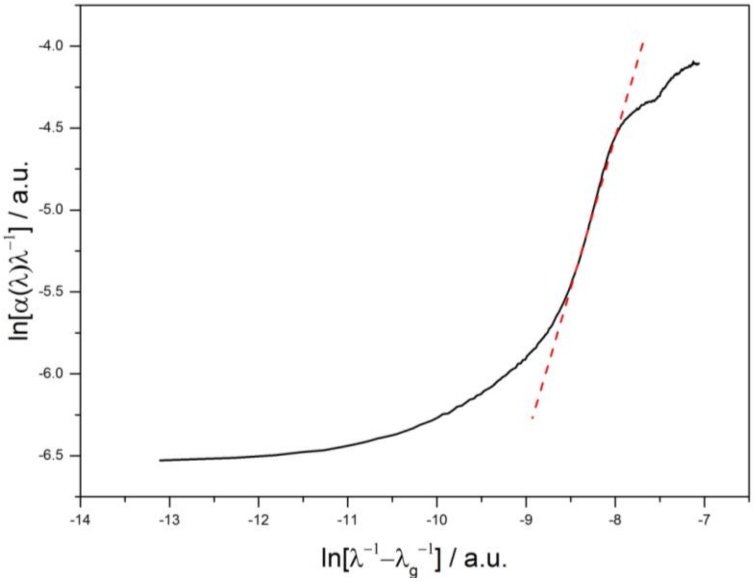

Fig. S12. Plot of $\ln[\alpha(\lambda)\lambda^{-1}]$ versus $\ln(\lambda^{-1} - \lambda_g^{-1})$ for the ZFO sample with $x = 0.074 \pm 0.011$. $\lambda_g = 614$ nm is the wavelength of the band gap transition. The value of the slope of the linear section of the graph indicates the nature of the optical carrier transition. A slope of 1.95 (≈ 2) is observed for the red dashed line, indicating an indirect allowed band gap. Identical results are found for the samples quenched at higher temperatures.

References

1 H. Ehrhardt, S. J. Campbell and M. Hofmann, Structural evolution of ball-milled $ZnFe_2O_4$, *J. Alloys Compd.*, 2002, **339**, 255–260.

2 F. Grandjean, G. J. Long, G. Longworth and B. J. Laundy, Iron-57 and Antimony-121 Mössbauer-Effect Study of Several Spinel Antimonates, *Inorg. Chem.*, 1984, **23**, 1886–1895.

3 T. Mizoguchi and M. Tanaka, The Nuclear Quadrupole Interaction of Fe^{57} in Spinel Type Oxides, *J. Phys. Soc. Japan*, 1963, **18**, 1301–1306.

4 A. Navrotsky and O. J. Kleppa, The thermodynamics of cation distributions in simple

spinels, *J. Inorg. Nucl. Chem.*, 1967, **29**, 2701–2714.

5 H. S. C. O’Neill and A. Navrotsky, Simple spinels: crystallographic parameters, cation radii, lattice energies, and cation distribution, *Am. Mineral.*, 1983, **68**, 181–194.

6 H. S. C. O’Neill and A. Navrotsky, Cation Distributions and Thermodynamic Properties of Binary Spinel Solid Solutions, *Am. Mineral.*, 1984, **69**, 733–753.

7 Z. Wang, D. Schiferl, Y. Zhao and H. S. C. O’Neill, High pressure Raman spectroscopy of spinel-type ferrite $ZnFe_2O_4$, *J. Phys. Chem. Solids*, 2003, **64**, 2517–2523.